InGaN-Based Lasers with an Inverted Ridge Waveguide Heterogeneously Integrated on Si(100)

Rui Zhou,[#] Meixin Feng,[#] Jin Wang, Qian Sun,* Jianxun Liu, Shuming Zhang, Masao Ikeda, Tong Liu, Zengli Huang, Xing Sheng, and Hui Yang

Read Online

ACCESS | Metrics & More | Article Recommendations | Supporting Information

ABSTRACT: Highly efficient electrically injected light source on exact Si(100) has been the bottleneck of Si photonics for decades. InGaN-based laser with a direct bandgap may serve as an efficient on-chip light source. But InGaN-based laser with a p-side ridge waveguide usually has a large electrical resistance and operation voltage, converting electricity into excessive Joule heat. The low wall plug efficiency, together with a large thermal resistance, leads to a high junction temperature, severely degrading device performance. Here, we proposed and fabricated a new laser structure with the ridge waveguide inverted from p-side to n-side. The differential electrical resistance and threshold voltage were slashed by 48% and 1.4 V, respectively. The thermal resistance and junction temperature were also reduced by 8 K/W and 25 °C, respectively. As a result, InGaN-based laser on exact Si(100) has been demonstrated under room-temperature continuous-wave current injection, which is fully compatible with Si-based microelectronics and a photonics platform.

KEYWORDS: InGaN-based laser, inverted ridge waveguide, electrical resistance and thermal resistance, GaN on Si, III nitride photonics
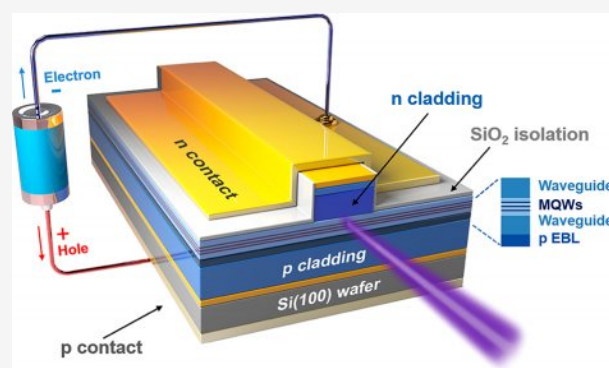
Silicon optoelectronic integrated circuits have been widely deemed as a promising solution to tackle the limitation of bandwidth and speed in computation and communication technologies.[1−3] However, Si with an indirect band structure usually cannot emit light efficiently. III-nitride semiconductors with a direct bandgap have a high luminous efficiency with an emission wavelength ranging from ultraviolet to infrared,[4] and have already been used for light-emitting diodes,[5] laser diodes (LDs),[6] and photonic integration with III-nitride or dielectric waveguide.[7,8] Therefore, III-nitride LDs may serve as an efficient on-chip light source for Si photonics.[9] To fully adopt the great advantages of Si-based mass-producing foundries, it is highly required to achieve InGaN-based laser on exact Si(100) under electrical injection.[10−12] In the previous work,[13−15] we have demonstrated InGaN-based LDs grown on Si(111) under room-temperature (RT) electrical injection, which however are less compatible with Si(100) complementary metal-oxide-semiconductor (CMOS). On the other hand, the electrical resistance and operation voltage of the reported InGaN-based LDs were relatively high,[13,14] converting electricity into excessive Joule heat, which greatly increased the junction temperature and degraded the device performance.

As a matter of fact, the large electrical resistance and thermal resistance are commonly observed for InGaN-based LDs, regardless of the substrate type and threading dislocation density (TDD). Even for the InGaN-based LDs grown on free-standing GaN substrates with a low TDD, the electrical resistance is also relatively large, resulting in a high operation voltage, which greatly reduces the Joule efficiency (<60%),[16,17] much lower than that of GaAs-based LDs (~90%).[18] Furthermore, the excessive Joule heat, together with the high thermal resistance, dramatically elevates the junction temperature, thus decreases the internal quantum efficiency (IQE) and wall plug efficiency (WPE). Therefore, even after decades of technological innovation, the WPE of the state-of-art InGaN-based LDs is still insufficient (<50%),[19] far below that of GaAs-based LDs (~80%).[18]

Ridge waveguide structure is widely adopted to confine the current injection and realize a high injection to reach population inversion for lasing. For InGaN-based LDs, ridge structure (~10 μm in width) is usually fabricated at the p-side surface, named as pRW-LDs, as shown in Figure 1a. The very limited hole injection area (10 × 800 μm²) combined with the high resistivity of p-type Ga(Al)N material gives a large electrical resistance for InGaN-based LDs. In fact, the effective
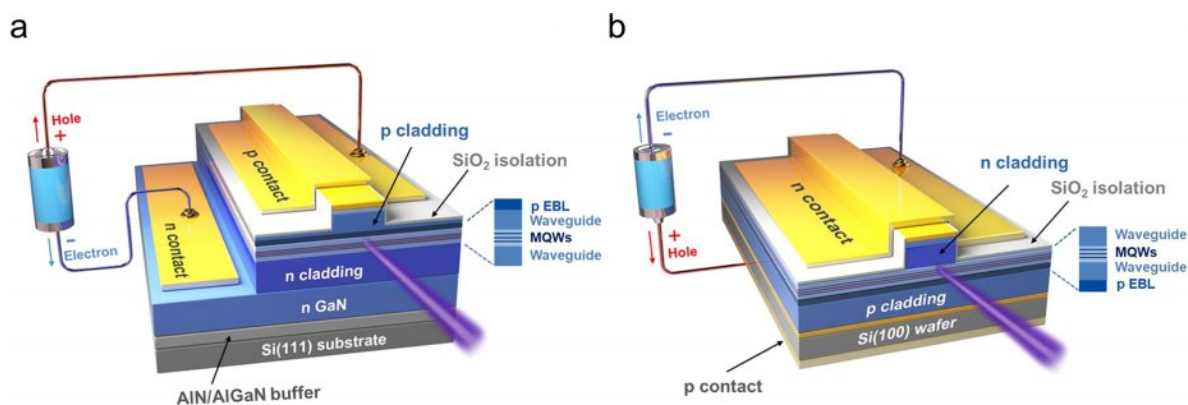
Figure 1. Schematic architecture of two laser structures. Schematic architecture of InGaN-based (a) pRW-LD on Si(111) and (b) nRW-LD on Si(100).
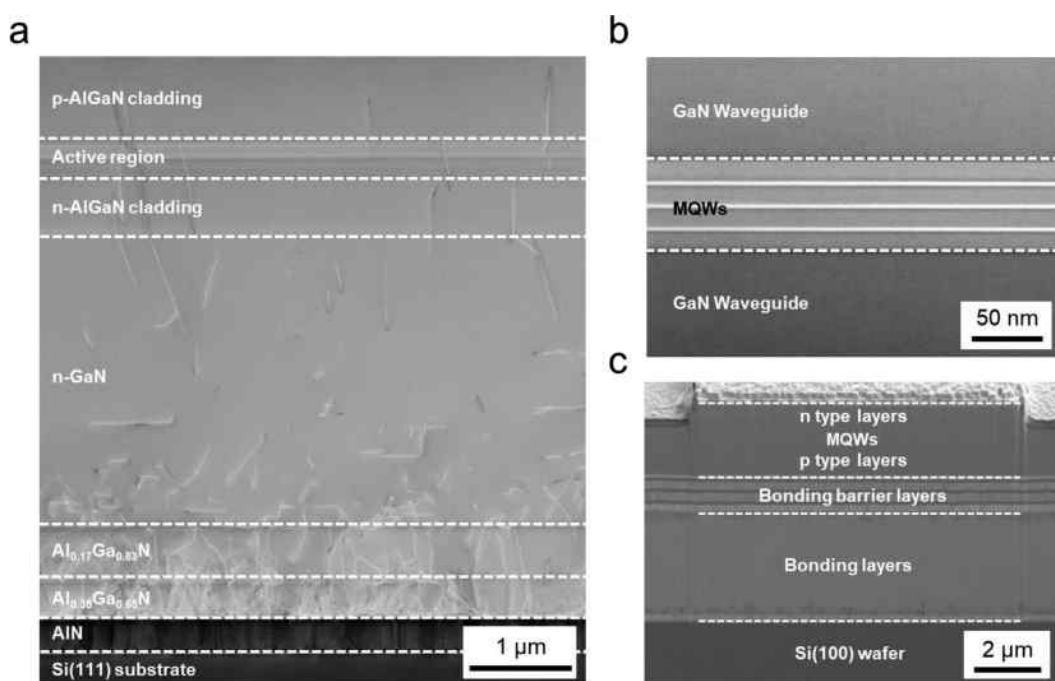

Figure 2. Cross-sectional images of nRW-LD structures. (a) Cross-sectional STEM image of the nRW-LD epitaxial structure grown on Si(111) substrate. (b) Enlarged image of the InGaN/GaN MQWs. (c) Cross-sectional scanning electron microscopy (SEM) image of the nRW-LD device on Si(100) wafer.

mass of holes in wide bandgap Ga(Al)N is much larger than that of electrons, which determines a very low mobility for holes (<10 cm^2/V·s)[20,21] much smaller than electron mobility ($\sim$150−1000 cm^2/V·s).[21] Meanwhile, the activation energy of Mg acceptor ($>$170 meV)[22] in Ga(Al)N is a lot higher than that of Si donor ($\sim$20 meV),[21] causing a low concentration of holes ($\sim$10^{17} cm^{-3}),[20,21] which is 1−2 orders of magnitude smaller than that of electrons ($\sim$10^{18}−10^{19} cm^{-3}).[21] Given the low concentration and low mobility of holes, the resistivity of p-type Ga(Al)N is 2−3 orders of magnitude larger than that of n-type Ga(Al)N, contributing to both the contact resistance and series resistance in the p-side ridge for hole injection.

On the other hand, p-side up package is usually adopted for InGaN-based LDs, because p-side down package often encounters various issues, including cavity facet contamination, short-circuit leakage, and so on.[23] The dissipation of Joule heat generated from the nonradiative recombination in the multiple quantum wells (MQWs) and the electrical resistance in the p-

type layers usually goes through the thick n-type AlGaN cladding layer and the AlGaN multilayer buffer with a low thermal conductivity, as well as the $\sim$100 μm thick substrate before reaching the heat sink, resulting in a large thermal resistance. The large thermal resistance and the excessive Joule heat in the InGaN-based pRW-LDs drive the junction to a high temperature and have a severely negative effect on the device performance.

To circumvent these issues and improve the WPE, InGaN-based LD with an n-side ridge waveguide (nRW-LD) is proposed of which the ridge structure is inverted from p-side to n-side, as shown in Figure 1b. Thanks to the very low resistivity of the n-type AlGaN cladding layer, the n-side electrical resistance changes very little for nRW-LDs. But nRW-LDs are blanketed with p-electrode, resulting in a substantially larger hole injection area (300 × 800 μm^2) than that of pRW-LDs. This greatly reduces the p-side contact resistance and series resistance, thereby slashing the operation

voltage and Joule heat. Moreover, nRW-LDs are p-side down bonded to the heatsink at the wafer level, which effectively shortens the heat dissipation path and cuts the thermal resistance. The reduction in both thermal resistance and Joule heat generation can effectively cool down the laser junction and hence improve the device performance. It should be mentioned that the p-side down bonding of nRW-LDs to the heat sink at the wafer level is distinctly different from individual chip bonding process, and can be massively processed for Si photonics integration with a good compatibility. In this work, InGaN-based nRW-LDs on exact Si(100) are carefully designed and successfully fabricated.

EXPERIMENTAL SECTION

The InGaN-based nRW-LDs were first epitaxially grown on Si(111) substrate, which matches Si(100) in both wafer size and thermal expansion coefficient, and can be fully compatible with the Si-based large-scale manufacturing foundries. Moreover, the Si(111) epitaxial substrate can be easily lift off by wet chemical etching with no damage, which facilitates the control of the n-side ridge depth from the N-face surface, given the full knowledge of the accurate thickness of the individual layers from the Si substrate (unlike the case of LDs grown on ∼300 μm thick GaN bulk substrate). Crack-free high-quality GaN templates with a low TDD were grown on Si(111) through critical stress engineering and defect control,[13,14] upon which a 5 μm thick crack-free InGaN-based laser structure was overgrown, including InGaN/GaN MQWs, waveguide, and cladding layers. In terms of the cross-sectional scanning transmission electron microscopy (STEM) images (Figure 2a), sharp interfaces of MQWs sandwiched by GaN waveguide layers were achieved (Figure 2b). It is worth mentioning that there was no Si doping in the 140 nm thick n-side waveguide layer and 50 nm thick AlGaN cladding layer near the n-side waveguide layer to suppress the undesired current spreading below the n-side ridge. In addition, InGaN-based conventional pRW-LDs were also grown on Si(111) substrate as a reference. The detailed structures were shown in the Section 1, Supporting Information.

The as-grown InGaN-based nRW-LD epitaxial structure with a blanketed p-type ohmic contact electrode was bonded to an exact Si(100) wafer, after that the Si(111) epitaxial substrate was eliminated by wet chemical etching.[24] Subsequently, the N-face n-type GaN surface was exposed after the AlN/AlGaN multilayer buffer was removed by dry etching. Afterward, the wafer was processed into Fabry−Pérot cavity laser devices with a ridge dimension of 10×800 μm². The cross-sectional view of the as-fabricated InGaN-based nRW-LD was shown in Figure 2c. The detailed fabrication process was summarized in Section 2, Supporting Information. The pRW-LD was also fabricated as a reference.[13]

It should be noted that it is not feasible to produce efficient InGaN-based nRW-LDs by overgrowing MQWs and n-type layers upon p-type layers, followed by the n-side ridge fabrication. This is because of the strong memory effect of Mg dopant, and the residual Mg impurities in the reaction chamber after the p-type layer growth may be unintentionally incorporated into the waveguide and MQWs, which would dramatically increase the optical absorption and decrease the IQE.[25] Moreover, it is very challenging to effectively activate the Mg acceptors in the buried p-type layer due to the high energy barrier of H atoms diffusion through n-type layer.[26,27] Therefore, the InGaN-based nRW-LD was prepared through

regular epitaxial growth, followed by wafer bonding and structure inversion for the n-side ridge fabrication.

Simulation of the optical field distribution for nRW-LD is shown in Figure S2, Supporting Information. It can be found that the majority of stimulated emission intensities were effectively confined in the MQWs and waveguide layers to enhance the optical gain, and the current spreading in nRW-LD was well suppressed, which is evidenced by the near-field patterns (NFPs; Figure S2c,d, Supporting Information). It is worth mentioning that the n-type AlGaN cladding layer of the nRW-LD was designed to be only 0.5 μm thick, much thinner than that (∼1.2 μm) of pRW-LD, due to the absence of antiguiding effect caused by the thick GaN template in conventional pRW-LD. The thickness reduction of the n-type AlGaN cladding layer with a low thermal conductivity can largely decrease both the thermal resistance and the tensile stress resulted from the lattice mismatch between AlGaN and GaN template, which boost the device performance and fabrication yield.

RESULTS AND DISCUSSION

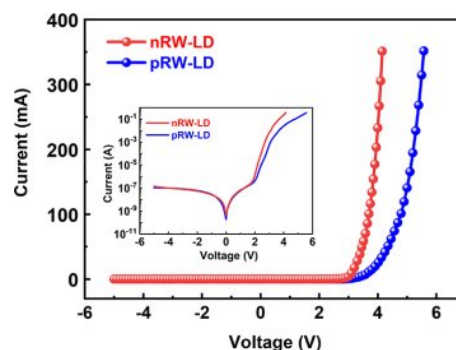The electrical characteristics of one as-fabricated nRW-LD on exact Si(100) were measured. Figure 3 presents the current

Figure 3. I−V characteristics of nRW and pRW LDs measured under various CW injection currents at RT. The inset shows the I−V curves are plotted in the logarithmic scale.

versus voltage (I−V) curves of the nRW-LD and pRW-LD under a continuous-wave (CW) current injection. The reverse leakage currents of the both devices were in the magnitude of 10^{-7} A under a reverse bias of −5 V, and the turn-on voltages were both around 3.0 V. When the voltage continued to increase, the I−V curve of the nRW-LD became much steeper and the current rose more rapidly than that of the pRW-LD, indicating that the electrical resistance of the nRW-LD was indeed much smaller than that of the pRW-LD.

For these two LDs, the ridge widths were both 10 μm, but the electrical current pathways were quite different. For the pRW-LD, the ridge structure was fabricated at the p-side, and the hole injection area was just 10 μm wide. In contrast, for the nRW-LD, due to the blanketed p-side electrode, the hole injection area was enlarged up to the whole chip dimension, resulting in a huge reduction in both p-type contact resistance and series resistance. At an injection current of 350 mA, the differential electrical resistance of the nRW-LD was 1.2 Ω, only 52% of that of the pRW-LD (2.3 Ω). Consequently, the operation voltage of the nRW-LD was only 4.15 V, which was 1.41 V lower than that of the pRW-LD (5.56 V). The huge drop in electrical resistance and operation voltage are of great

benefits to diminishing the Joule heat generation, cooling down the laser junction, and hence improving the device performance.

The junction temperature and thermal resistance of the as-fabricated nRW-LD and pRW-LD were measured to study the thermal characteristics. The experimental measurements were carried out based on the forward-voltage method, which is according to the linear relationship between the reciprocal of absolute temperature $(1/T)$ and natural logarithm of the forward voltage subtracted by the turn-on voltage at a given injection current. A more specific description of this measurement method can be found in refs 28 and 29 and Section 4, Supporting Information. Figure 4 shows the linear dependence
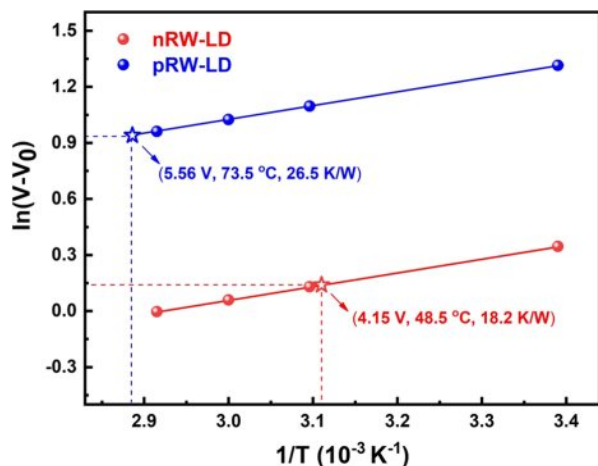

Figure 4. Plot of $\ln(V - V_0)$ as a function of reciprocal of absolute temperature $(1/T)$ at an injection current of 350 mA. Measurement was performed under a pulsed current injection with 0.1% duty cycle and a 0.1 μs pulse width. The red and blue solid balls represent the measured values at various ambient temperature (22, 50, 60, and 70 °C). The red and blue solid lines are the linear fitting curves of nRW-LD and pRW-LD, respectively. Under a CW injection current of 350 mA, the operation voltage, junction temperature, and thermal resistance of nRW-LD and pRW-LD were labeled in the figure and indicated by red and blue pentagrams, respectively.

of $\ln(V - V_0)$ on $1/T$ for the nRW-LD and pRW-LD at an injection current of 350 mA. When the heat sink was maintained at the ambient temperature, the junction temperature of these two devices under a CW current injection can be calculated according to the calibration curves and the measured forward voltage. For the as-fabricated nRW-LD and pRW-LD, the operation voltages at a CW current of 350 mA were 4.15 and 5.56 V, and the junction temperatures were 48.5 and 73.5 °C, respectively, as shown in Figure 4. The corresponding thermal resistances were calculated to be 18.2 and 26.5 K/W, respectively. The junction temperature and the thermal resistance of the nRW-LD were 25 °C and 8 K/W lower than those of the pRW-LD, which was mainly due to the huge reduction in Joule heat generation and the shortened heat dissipation path (no AlGaN-based multilayer buffer with a low thermal conductivity) for the nRW-LD. It is noted that we have also carried out threshold-current method to examine the junction temperature. Measurement results show a good agreement with the data obtained by the forward-voltage method, implying a good validity and accuracy of the forward-voltage method. More details can be found in Section 4, Supporting Information.

For InGaN-based nRW-LDs, the wafer bonding material plays a very important role in heat dissipation. A simulation study based on the finite element method was carried out for both the nRW-LD and the pRW-LD. The detailed parameters of thermal conductivity and thickness for each layer were presented in Section 6, Supporting Information. As shown in Table 1, the simulation results were quite consistent with the

Table 1. Measured and Simulated Thermal Characteristics of nRW-LD and pRW-LD

thermal characteristics	measurement		simulation		
	pRW-LD	nRW-LD	pRW-LD	nRW-LD	nRW-LD
bonding layers		Ni−Sn		Ni−Sn	copper
junction temperature (°C)	73.5	48.5	74.1	48.7	41.2
thermal resisitance (K/W)	26.5	18.2	26.8	18.4	13.2

experimental data, confirming the superiority of the nRW-LDs in thermal resistance and junction temperature over the conventional pRW-LDs. Ni−Sn solder with a low thermal conductivity was adopted for the wafer bonding of the nRW-LD with Si(100) wafer in this work, which made a substantial contribution to the thermal resistance of the as-fabricated nRW-LD. In future work, Ni−Sn solder can be replaced by materials with a high thermal conductivity to greatly reduce the thermal resistance of nRW-LDs. Cu with high thermal conductivity is widely used for CMOS manufacturing, and can be a good candidate. Wafer bonding technology based on Cu-to-Cu compatible with CMOS has already been reported.[30] Simulation results indicate that the thermal resistance of nRW-LDs can be further reduced by another one-third to 13.2 K/W by using copper solder, which can fully release the huge potential of nRW-LDs in thermal characteristics.

Figure 5 reveals the optoelectronic characteristics of one as-fabricated nRW-LD at RT. The normalized electroluminescence (EL) spectra of the nRW-LD were tested as Figure 5a exhibited. The laser device showed a spontaneous emission spectrum with a full width at half-maximum (fwhm) of 12 nm at 100 mA. When the injection current increased to the threshold current of 320 mA, the fwhm of the emission spectrum was sharply decreased to 0.8 nm, as well as the stimulated emission at 418.3 nm was observed as shown in Figure 5b. And the far-field patterns (FFPs) of the nRW-LD were recorded in Figure 5c,d at the injection currents of 0.8 I_{th} and 1.2 I_{th}, respectively. After exceeding the threshold, a typical elliptical FFP was clearly observed. Figure 5e exhibits the EL output power of the nRW-LD under various injection currents at RT, and the explicit turning points at 320 and 350 mA were observed in the plots of the light output power versus pulse and CW injection currents, respectively. All of the above results, as well as the NFP observations (Figure S2c,d, Supporting Information), are clear signatures of electrically injected lasing at RT. It should be mentioned that the negligible difference in threshold current between pulsed and CW modes (Figure 5e) is a direct reflection of the good control of the device operating junction temperature for the nRW-LD. In addition, a series of fabricated nRW-LDs were measured regarding the threshold current, with the statistical results shown in Figure S4, Supporting Information, presenting a decent yield and reproducibility.
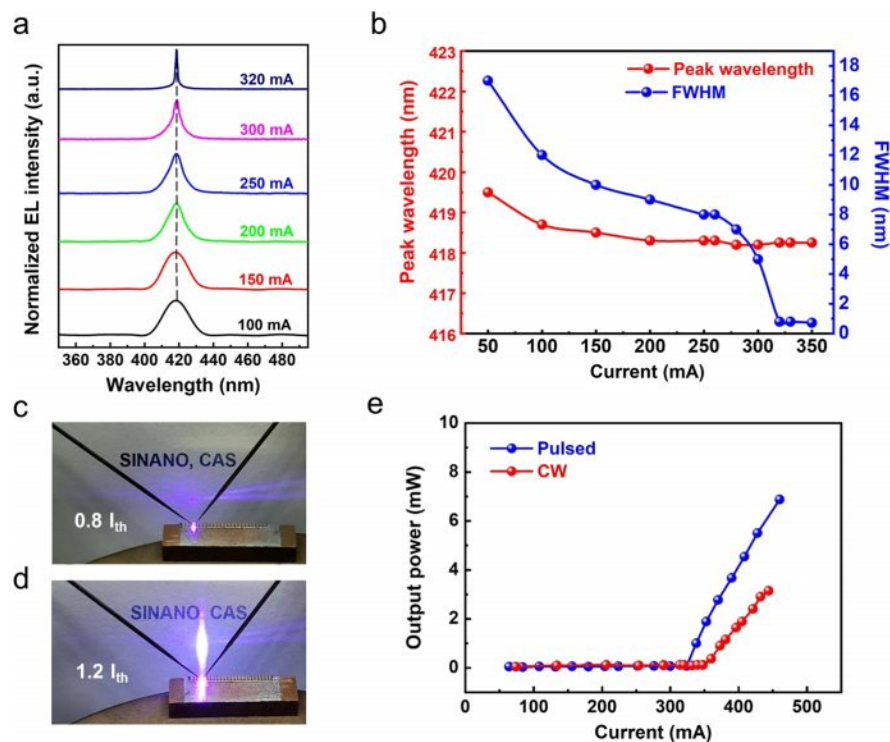
Figure 5. EL characteristics of nRW-LD under electrical injection. (a) EL spectra tested under various pulsed currents (a 0.4% duty cycle with a 10 kHz repetition rate) at RT. (b) Peak wavelength and fwhm of the EL spectra with the relationship of the pulsed injection at RT. (c, d) FFPs observed 0.8 I_{th} and 1.2 I_{th}, respectively. (e) Light output power as a function of the pulsed and CW injection current at RT for one simply packaged nRW-LD.

It should be mentioned that the threshold current density (4.37 kA/cm^2) of the as-fabricated nRW-LD under CW current injection at RT is relatively high as compared to the state-of-art InGaN-based LD, and the CW operation lifetime of nRW-LDs was measured to be 5 min before a drastic degradation of output power. The reason for the relatively high threshold current and limited lifetime is mainly due to the relatively high TDD of ~6 × 10^8 cm^{-2} and the unoptimized active region. It has been reported that TDs greatly affect both the IQE as nonradiative recombination centers and the injection efficiency by forming a leakage path.[31,32] Additionally, TDs may assist the diffusion of impurities and other point defects into the MQWs, causing a further drop in IQE, thus an increase in threshold current density.[33] On the other hand, the active region structure and growth conditions are to be optimized for the InGaN-based nRW-LDs. The thermal degradation of the MQWs during the p-type layers overgrowth at high temperature often induces group-III vacancies (V_{Ga} and V_{In}) defects and metallic In precipitates, especially in the presence of large strain field and the high density of TDs in the LD active region. The vacancies and metallic In precipitates act as efficient channels for nonradiative recombination and optical absorption centers, and hence, greatly affect the IQE and threshold current density.[34] According to the literature, when the TDD in the InGaN-based laser epilayer is cut down from 10^8 to 10^6 cm^{-2}, the device lifetime can be lengthened to over 10000 h.[35] A further study of reducing the TDD and optimizing the active region of nRW-LDs is expected to greatly improve the device performance given the excellent control of electrical and thermal resistance.

CONCLUSION

In summary, the InGaN-based laser with an inverted ridge waveguide on exact Si(100) has been demonstrated under CW current injection at RT. As a result of inverting the ridge structure from the conventional p-side to the n-side, the differential electrical resistance and threshold voltage dropped by 48% and 1.4 V, respectively, and the thermal resistance and junction temperature were reduced by 8 K/W and 25 °C, respectively. The experimental data agree well with the simulation results, and the simulation study indicates that the thermal resistance can be reduced by another one-third, when replacing the Ni−Sn bonding material with highly thermal conductive copper. With a boost in InGaN-based LD material quality and adoption of better bonding material with a high thermal conductivity, the device performance of nRW-LDs can be further improved. Moreover, InGaN-based nRW-LDs on exact Si(100) are fully compatible with the large-scale Si-based CMOS platform and can be utilized in monolithically integrated Si photonics as an efficient on-chip light source.

METHODS

Material Growth. The InGaN-based laser materials were epitaxially grown on Si by metal−organic vapor phase epitaxy. The precursors of nitrogen, indium, gallium, and aluminum were ammonia, trimethylindium, trimethylgallium, and trimethylaluminum, respectively. And the dopants of p- and n-type were carried out with bis-cyclopentadienyl magnesium and monosilane, respectively. Upon a Si(111) substrate, the carefully designed buffer, including the AlN/Al$_{0.35}$Ga$_{0.65}$N/Al$_{0.17}$Ga$_{0.83}$N multilayer with a thickness of 300/300/400 nm, was grown prior to the 2.6 μm thick crack-free GaN template. On the GaN template, InGaN-based nRW-LD structure was

overgrown, containing a 450 nm thick n-type $Al_{0.08}Ga_{0.92}N$ cladding layer (CL), a 50 nm thick undoped $Al_{0.08}Ga_{0.92}N$ CL, 140 nm thick undoped GaN waveguide (WG), MQW structures consisted of three pairs of undoped $In_{0.12}Ga_{0.88}N$ QW and $In_{0.02}Ga_{0.98}N$ barrier layer with the thicknesses of 2.5 and 12 nm, respectively, a 90 nm thick undoped GaN WG, an electron blocking layer (EBL) composed of 20 nm thick p-type $Al_{0.18}Ga_{0.82}N$, a 600 nm thick p-type $Al_{0.07}Ga_{0.93}N$ CL, and a 30 nm thick p-type GaN contact layer.

Device Fabrication. The schematic diagrams illustrating the detailed device fabrication process are shown in the Figure S1, Supporting Information. The laser wafer was fabricated into laser devices with a ridge dimension of $10 \times 800 \ \mu m^2$. The cavity mirrors were first formed by inductively coupled plasma etching, and then refined by a FEI Scios Dual-Beam focus ion beam equipped with an SEM to improve the verticality and the smoothness. After that, in order to reduce the mirror loss, the front and the rear facets of the nRW-LDs were coated by quarter-wave SiO_2/Ta_2O_5 highly reflective films with five and nine pairs, respectively.

Characterization. FEI Tecnai S-Twin TEM and FEI Quanta 400 SEM were performed for recording STEM and SEM images, respectively. An KEITHLEY-2400 SourceMeter analyzer was used for electrical measurements. An optical power meter (Thorlabs PM121D) and a calibrated integrating sphere were utilized for the light output power under CW and pulsed injection, respectively. A CCD spectrometer (Idea Optics FX4000) was used to test the EL spectra.

ASSOCIATED CONTENT

Supporting Information

The Supporting Information is available free of charge at https://pubs.acs.org/doi/10.1021/acsphotonics.0c01061.

> Section 1, The detailed epitaxial structures of the nRW-LD and pRW-LD wafers; Section 2, The device fabrication process of the nRW-LDs; Section 3, The optical field distribution of nRW-LDs; Section 4, The detailed description for the measurement of junction temperature; Section 5, The statistic measurement results of the threshold current of nRW-LDs; Section 6, The detailed information on simulation study about thermal characteristics (PDF)

AUTHOR INFORMATION

Corresponding Author

Qian Sun − *Key Laboratory of Nanodevices and Applications, Suzhou Institute of Nano-Tech and Nano-Bionics (SINANO), Chinese Academy of Sciences (CAS), Suzhou 215123, China; School of Nano-Tech and Nano-Bionics, University of Science and Technology of China, Hefei 230026, China; Guangdong (Foshan) Branch, SINANO, CAS, Foshan 528000, China;* orcid.org/0000-0001-5495-2232; Email: qsun2011@sinano.ac.cn

Authors

Rui Zhou − *Key Laboratory of Nanodevices and Applications, Suzhou Institute of Nano-Tech and Nano-Bionics (SINANO), Chinese Academy of Sciences (CAS), Suzhou 215123, China; School of Nano-Tech and Nano-Bionics, University of Science and Technology of China, Hefei 230026, China;* orcid.org/0000-0003-1786-5994

Meixin Feng − *Key Laboratory of Nanodevices and Applications, Suzhou Institute of Nano-Tech and Nano-Bionics (SINANO), Chinese Academy of Sciences (CAS), Suzhou 215123, China; School of Nano-Tech and Nano-Bionics, University of Science and Technology of China, Hefei 230026, China; Guangdong (Foshan) Branch, SINANO, CAS, Foshan 528000, China;* orcid.org/0000-0002-3206-6990

Jin Wang − *Key Laboratory of Nanodevices and Applications, Suzhou Institute of Nano-Tech and Nano-Bionics (SINANO), Chinese Academy of Sciences (CAS), Suzhou 215123, China;* orcid.org/0000-0003-3098-4138

Jianxun Liu − *Key Laboratory of Nanodevices and Applications, Suzhou Institute of Nano-Tech and Nano-Bionics (SINANO), Chinese Academy of Sciences (CAS), Suzhou 215123, China;* orcid.org/0000-0001-8485-166X

Shuming Zhang − *Key Laboratory of Nanodevices and Applications, Suzhou Institute of Nano-Tech and Nano-Bionics (SINANO), Chinese Academy of Sciences (CAS), Suzhou 215123, China; School of Nano-Tech and Nano-Bionics, University of Science and Technology of China, Hefei 230026, China; Guangdong (Foshan) Branch, SINANO, CAS, Foshan 528000, China*

Masao Ikeda − *Key Laboratory of Nanodevices and Applications, Suzhou Institute of Nano-Tech and Nano-Bionics (SINANO), Chinese Academy of Sciences (CAS), Suzhou 215123, China*

Tong Liu − *Vacuum Interconnected Nanotech Workstation, SINANO, CAS, Suzhou 215123, China;* orcid.org/0000-0001-7175-8896

Zengli Huang − *Vacuum Interconnected Nanotech Workstation, SINANO, CAS, Suzhou 215123, China*

Xing Sheng − *Department of Electronic Engineering, Tsinghua University, Beijing 100084, China;* orcid.org/0000-0002-8744-1700

Hui Yang − *Key Laboratory of Nanodevices and Applications, Suzhou Institute of Nano-Tech and Nano-Bionics (SINANO), Chinese Academy of Sciences (CAS), Suzhou 215123, China; School of Nano-Tech and Nano-Bionics, University of Science and Technology of China, Hefei 230026, China; Guangdong (Foshan) Branch, SINANO, CAS, Foshan 528000, China; Vacuum Interconnected Nanotech Workstation, SINANO, CAS, Suzhou 215123, China*

Complete contact information is available at:
https://pubs.acs.org/10.1021/acsphotonics.0c01061

Author Contributions

[#]The authors contributed equally to this work.

Notes

The authors declare no competing financial interest.

ACKNOWLEDGMENTS

■ REFERENCES

(1) Hirschman, K. D.; Tsybeskov, L.; Duttagupta, S. P.; Fauchet, P. M. Silicon-based visible light-emitting devices integrated into microelectronic circuits. *Nature* **1996**, *384*, 338−341.

(2) Sun, C.; Wade, M. T.; Lee, Y.; Orcutt, J. S.; Alloatti, L.; Georgas, M. S.; Waterman, A. S.; Shainline, J. M.; Avizienis, R. R.; Lin, S.; Moss, B. R.; Kumar, R.; Pavanello, F.; Atabaki, A. H.; Cook, H. M.; Ou, A. J.; Leu, J. C.; Chen, Y. H.; Asanovic, K.; Ram, R. J.; Popovic, M. A.; Stojanovic, V. M. Sing-chip microprocessor that communicates directly using light. *Nature* **2015**, *528*, 534−538.

(3) Atabaki, A. H.; Moazeni, S.; Pavanello, F.; Gevorgyan, H.; Notaros, J.; Alloatti, L.; Wade, M. T.; Sun, C.; Kruger, S. A.; Meng, H. Y.; Al Qubaisi, K.; Wang, I.; Zhang, B. H.; Khilo, A.; Baiocco, C. V.; Popovic, M. A.; Stojanovic, V. M.; Ram, R. J. Integrating photonics with silicon nanoelectronics for the next generation of systems on a chip. *Nature* **2018**, *556*, 349−354.

(4) Jain, S. C.; Willander, M.; Narayan, J.; Van Overstraeten, R. III-nitrides: Growth, characterization, and properties. *J. Appl. Phys.* **2000**, *87*, 965−1006.

(5) Pimputkar, S.; Speck, J. S.; DenBaars, S. P.; Nakamura, S. Prospects for LED lighting. *Nat. Photonics* **2009**, *3*, 180−182.

(6) Hardy, M. T.; Feezell, D. F.; DenBaars, S. P.; Nakamura, S. Group III-nitride lasers: a materials perspective. *Mater. Today* **2011**, *14* (9), 408−415.

(7) Wang, Y. J.; Wang, X.; Zhu, B. C.; Shi, Z.; Yuan, J. L.; Gao, X. M.; Liu, Y. H.; Sun, X. J.; Li, D. B.; Amano, H. Full-duplex light communication with a monolithic multicomponent system. *Light: Sci. Appl.* **2018**, *7*, 83.

(8) Li, K. H.; Fu, W. Y.; Cheung, Y. F.; Wong, K. K. Y.; Wang, Y.; Lau, K. M.; Choi, H. W. Monolithically integrated InGaN/GaN light-emitting diodes, photodetectors, and waveguides on Si substrate. *Optica* **2018**, *5*, 564−569.

(9) Zhou, Z. P.; Yin, B.; Michel, J. On-chip light sources for silicon photonics. *Light: Sci. Appl.* **2015**, *4*, e358.

(10) Zhou, T. J.; Tang, M. C.; Xiang, G. H.; Xiang, B. Y.; Hark, S.; Martin, M.; Baron, T.; Pan, S. J.; Park, J. S.; Liu, Z. Z.; Chen, S. M.; Zhang, Z. Y.; Liu, H. Y. Continuous-wave quantum dot photonic crystal lasers grown on axis Si(001). *Nat. Commun.* **2020**, *11*, 977.

(11) Rio Calvo, M.; Monge Bartolome, L.; Bahriz, M.; Boissier, G.; Cerutti, L.; Rodriguez, J.-B.; Tournie, E. Mid-infrared laser diodes epitaxially grown on on-axis (001) silicon. *Optica* **2020**, *7*, 263−266.

(12) Shi, B.; Zhao, H.; Wang, L.; Song, B.; Suran Brunelli, S. T.; Klamkin, J. Continuous-wave electrically pumped 1550 nm lasers epitaxially grown on on-axis (001) silicon. *Optica* **2019**, *6*, 1507−1514.

(13) Sun, Y.; Zhou, K.; Sun, Q.; Liu, J. P.; Feng, M. X.; Li, Z. C.; Zhou, Y.; Zhang, L. Q.; Li, D. Y.; Zhang, S. M.; Ikeda, M.; Liu, S.; Yang, H. Room-temperature continuous-wave electrically injected InGaN-based laser directly grown on Si. *Nat. Photonics* **2016**, *10*, 595−599.

(14) Sun, Y.; Zhou, K.; Feng, M. X.; Li, Z. C.; Zhou, Y.; Sun, Q.; Liu, J. P.; Zhang, L. Q.; Li, D. Y.; Sun, X. J.; Li, D. B.; Zhang, S. M.; Ikeda, M.; Yang, H. Room-temperature continuous-wave electrically pumped InGaN/GaN quantum well bule laser diode directly grown on Si. *Light: Sci. Appl.* **2018**, *7*, 13.

(15) Feng, M. X.; Li, Z. C.; Wang, J.; Zhou, R.; Sun, Q.; Sun, X. J.; Li, D. B.; Gao, H. W.; Zhou, Y.; Zhang, S. M.; Li, D. Y.; Zhang, L. Q.; Liu, J. P.; Wang, H. B.; Ikeda, M.; Zheng, X. H.; Yang, H. Room-Temperature Electrically Injected AlGaN-Based near-Ultraviolet Laser Grown on Si. *ACS Photonics* **2018**, *5*, 699−704.

(16) Piprek, J. Comparative analysis of GaN-based light-emitting diodes and laser diodes. *Appl. Phys. Lett.* **2016**, *109*, No. 021104.

(17) Piprek, J. Internal power loss in GaN-based lasers: mechanisms and remedies. *Opt. Quantum Electron.* **2017**, *49*, 329.

(18) Yuan, G.; Xiong, K. L.; Zhang, C.; Li, Y. F.; Han, J. Optical engineering of Modal gain in a III-nitride laser with Nanoporous GaN. *ACS Photonics* **2016**, *3*, 1604−1010.

(19) Nakatsu, Y.; Nagao, Y.; Hirao, T.; Hara, Y.; Masui, S.; Yanamoto, T.; Nagahama, S. Blue and green InGaN semiconductor lasers as light sources for displays. *Proc. SPIE* **2020**, *11280*, 26.

(20) Nakamura, S.; Mukai, T.; Senoh, M.; Iwasa, N. Thermal annealing effects on p-type Mg-doped GaN films. *Jpn. J. Appl. Phys.* **1992**, *31*, L139−L142.

(21) Sheu, J. K.; Chi, G. C. The doping process and dopant characteristics of GaN. *J. Phys.: Condens. Matter* **2002**, *14*, R657−R702.

(22) Gotz, W.; Johnson, N. M.; Walker, J.; Bour, D. P.; Street, R. A. Activation of acceptors in Mg-doped GaN grown by metalorganic chemical vapor deposition. *Appl. Phys. Lett.* **1996**, *68*, 667−669.

(23) Zhang, Z. Q.; Wong, C. P. Recent advances in flip-chip underfill: Materials, process, and reliability. *IEEE Trans. Adv. Packag.* **2004**, *27*, 515−524.

(24) Sun, Q.; Yan, W.; Feng, M. X.; Li, Z. C.; Feng, B.; Zhao, H. M.; Yang, H. GaN-on-Si blue/white LEDs: epitaxy, chip, and package. *J. Semicond.* **2016**, *37*, No. 044006.

(25) Xing, H. L.; Green, D. S.; Yu, H. J.; Mates, T.; Kozodoy, P.; Keller, S.; Denbaars, S. P.; Mishra, U. K. Memory effect and redistribution of Mg into sequentially regrown GaN layer by metalorganic chemical vapor deposition. *Jpn. J. Appl. Phys.* **2003**, *42*, 50−53.

(26) Neugebauer, J.; Van De Walle, C. G. Hydrogen in GaN: novel aspects of a common impurity. *Phys. Rev. Lett.* **1995**, *75*, 4452−4455.

(27) Czernecki, R.; Grzanka, E.; Jakiela, R.; Grzanka, S.; Skierbiszewski, C.; Turski, H.; Perlin, P.; Suski, T.; Donimirski, K.; Leszczynski, M. Hydrogen diffusion in GaN: Mg and GaN: Si. *J. Alloys Compd.* **2018**, *747*, 354−35.

(28) Xi, Y.; Schubert, E. R. Junction-temperature measurement in GaN ultraviolet light-emitting diodes using diode forward voltage method. *Appl. Phys. Lett.* **2004**, *85*, 2163−2165.

(29) Feng, M. X.; Zhang, S. M.; Jiang, D. S.; Liu, J. P.; Wang, H.; Zeng, C.; Li, Z. C.; Wang, H. B.; Wang, F.; Yang, H. Thermal characterization of GaN-based laser diodes by forward-voltage method. *J. Appl. Phys.* **2012**, *111*, No. 094513.

(30) Huang, Y.-P.; Chien, Y.-S.; Tzeng, R.-N.; Shy, M.-S.; Lin, T.-H.; Chen, K.-H.; Chiu, C.-T.; Chiou, J.-C.; Chuang, C.-T.; Hwang, W.; Tong, H.-M.; Chen, K.-N. Novel Cu-to-Cu bonding with Ti passivation at 180 °C in 3-D integration. *IEEE Electron Device Lett.* **2013**, *34*, 1551−1553.

(31) Hino, T.; Tomiya, S.; Miyajima, T.; Yanashima, K.; Hashimoto, S.; Ikeda, M. Characterization of threading dislocations in GaN epitaxial layers. *Appl. Phys. Lett.* **2000**, *76*, 3421−3423.

(32) Tomiya, S.; Hino, T.; Goto, S.; Takeya, M.; Ikeda, M. Dislocation related issues in the degradation of GaN-based laser diodes. *IEEE J. Sel. Top. Quantum Electron.* **2004**, *10*, 1277−1286.

(33) Marona, L.; Wisniewski, P.; Prystawko, P.; Grzegory, I.; Suski, T.; Porowski, S.; Perlin, P.; Czernecki, R.; Leszczynski, M. Degradation mechanisms in InGaN laser diodes grown on bulk GaN crystals. *Appl. Phys. Lett.* **2006**, *88*, 201111.

(34) Dreyer, C. E.; Alkauskas, A.; Lyons, J. L.; Speck, J. S.; Van de Walle, C. G. Gallium vancancy complexes as a cause of Shockley-Read-Hall recombination in III-nitride light emitters. *Appl. Phys. Lett.* **2016**, *108*, 141101.

(35) Nakamura, S. The roles of structural imperfections in InGaN-based blue light-emitting diodes and laser diodes. *Science* **1998**, *281*, 956−961.

Supporting Information

InGaN-based lasers with an inverted ridge waveguide heterogeneously integrated on Si(100)

Authors: Rui Zhou[1,2#], Meixin Feng[1,2,3#], Jin Wang[1], Qian Sun[1,2,3*], Jianxun Liu[1], Shuming Zhang[1,2,3], Masao Ikeda[1], TongLiu[4], Zengli Huang[4], Xing Sheng[5], and Hui Yang[1,2,3,4]

Affiliations:

[1]*Key Laboratory of Nanodevices and Applications, Suzhou Institute of Nano-Tech and Nano-Bionics (SINANO), Chinese Academy of Sciences (CAS), Suzhou 215123, China*

[2]*School of Nano-Tech and Nano-Bionics, University of Science and Technology of China, Hefei 230026, China*

[3]*Guangdong (Foshan) Branch, SINANO, CAS, Foshan, 528000, China*

[4]*Vacuum Interconnected Nanotech Workstation, SINANO, CAS, Suzhou 215123, China*

[5]*Department of Electronic Engineering, Tsinghua University, Beijing 100084, China*

[#]*Contributed equally to this work.*

Correspondence to: qsun2011@sinano.ac.cn

This file contains:

Section 1. The detailed epitaxial structures of the nRW-LD and pRW-LD wafers.

Section 2. The device fabrication process of the nRW-LDs.

Section 3. The optical field distribution of nRW-LDs.

Section 4. The detailed description for the measurement of junction temperature.

Section 5. The statistic measurement results of the threshold currents of nRW-LDs.

Section 6. The detailed information of simulation study about thermal characteristics.

Section 1: The detailed epitaxial structures of the nRW-LD and pRW-LD wafers.

Table S1: Detailed epitaxial structures of the nRW-LD and pRW-LD.

Structure	nRW-LD		pRW-LD	
	Material	Thickness (nm)	Material	Thickness (nm)
p-contact	p-GaN	30	The same as nRW-LD	
p-cladding	p-Al$_{0.07}$Ga$_{0.93}$N	600		
EBL	p-Al$_{0.18}$Ga$_{0.82}$N	20		
Waveguide	u-GaN	90		
3 QWs	QW: u-In$_{0.12}$Ga$_{0.88}$N	2.5		
	QB: u-In$_{0.02}$Ga$_{0.98}$N	12		
Waveguide	u-GaN	140	n-GaN	100
n-cladding	u-Al$_{0.08}$Ga$_{0.92}$N	50	n-Al$_{0.08}$Ga$_{0.92}$N	1200
	n-Al$_{0.08}$Ga$_{0.92}$N	450		
n-contact	n-GaN	1300	The same as nRW-LD	
Templates	GaN	1300	The same as nRW-LD	
	Al$_{0.17}$Ga$_{0.83}$N	400		
	Al$_{0.35}$Ga$_{0.65}$N	300		
	AlN	300		

Upon a thermally cleaned Si(111) substrate, 2.6-μm-thick crack-free high-quality

GaN template was grown with a 300-nm-thick AlN nucleation layer and an Al-

composition step-graded AlGaN multilayer buffer consisting of a 300-nm-thick $Al_{0.35}Ga_{0.65}N$ layer and a 400-nm-thick $Al_{0.17}Ga_{0.83}N$ layer. Afterwards, InGaN-based nRW-LD and pRW-LD structures were overgrown. The detailed epitaxial structure information of both the devices was shown in Table S1.

The epitaxial structure of the nRW-LD was the same as that of pRW-LD, except the n-side AlGaN cladding layer and GaN waveguide layer. The thickness of n-side GaN waveguide was increased to 140 nm, and the thickness of n-type AlGaN cladding layer was reduced from 1200 to 500 nm due to the absence of the anti-waveguide effect. In the nRW-LD structure, the 140-nm-thick n-side waveguide layer and 50-nm-thick n-side AlGaN cladding layer near the waveguide layer were undoped to suppress the current spreading below the n-side ridge. The as-fabricated nRW-LDs had a vertical structure with p- and n-contact at the opposite sides, while the pRW-LDs had a lateral structure with both p- and n-contacts at the same side.

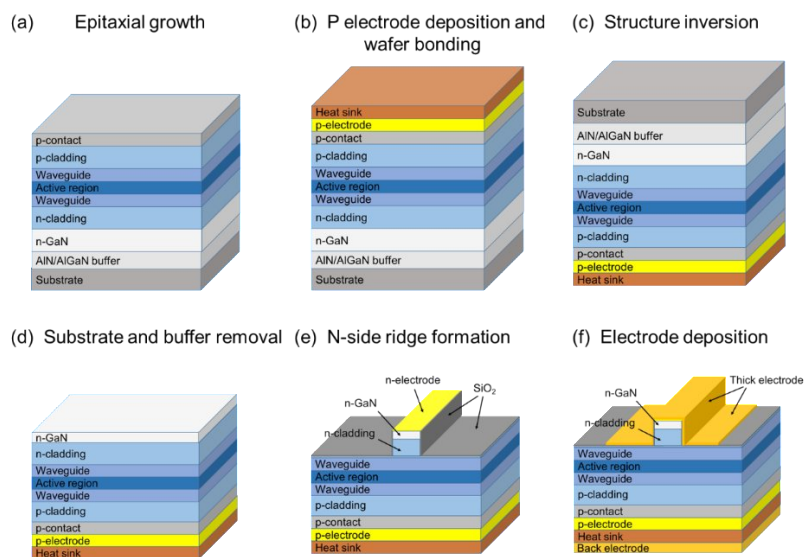Section 2: The device fabrication process of the InGaN-based nRW-LDs.

Figure S1: Schematic diagram illustrating the fabrication process of nRW-LD. (a) An inverted ridge waveguide laser epitaxial structure was grown on Si(111) substrate. (b) Ohmic contact metal stack Pd/Pt/Au was sputtered on p-type GaN contact layer followed by a thermal annealing, and subsequently the wafer was bonded to a Si(100) wafer. (c) The structure was inverted after wafer bonding process. (d) Wet chemical etching and dry etching were used to remove the Si(111) substrate, AlN/AlGaN buffer and u-GaN, respectively. After that, n-type GaN contact layer was exposed. (e)　Ohmic contact metal stack Ti/Pt/Au was sputtered on the n-type GaN contact layer by a magnetron sputtering, and then lithography process and dry etching were used to form the ridge structure. Afterwards, SiO$_2$ isolation layer was deposited on the wafer, and a lift-off technique was used to expose the metal stack Ti/Pt/Au. (f) Lithography, deposition and lift-off processes were used to form Ti/Pt/Au pad. The Si(100) wafer thickness was reduced to around 90 μm by thinning, lapping, and chemical mechanical polishing, and then back-side electrode Cr/Pd/Au was deposited on Si(100) wafer by a magnetron sputtering.

Section 3: The optical field distribution of nRW-LDs.

The optical field distribution of the nRW-LD was simulated by the beam propagation method. Figure S2a shows the refractive index profile and the calculated optical filed distribution along the vertical direction for the nRW-LD. It is noted that the thickness of the n-side waveguide layer was intentionally larger than that of the p-side waveguide layer, shifting the optical field towards the n-type layers to reduce the

internal optical loss induced by the strong absorption of Mg-doped p-type layers. Figure S2b shows the simulated optical field distribution at the cavity facet. With the proper design of the waveguide and cladding layers, most of optical field can be well confined within the active region.

Cross-sectional near-filed patterns (NFPs) of one as-fabricated nRW-LD were studied by using an optical microscope from the front facet at a current injection of below (Figure S2c) and above the threshold current (Figure S2d). When the injection current reached the threshold, strong stimulated emission was clearly observed from the front facet below the ridge, which was consistent with the simulation result (Figure S2b). It should be pointed out that for the as-fabricated nRW-LDs, the observed NFPs did not spread beyond the ridge width, indicating that the undesired current spreading in the n-side waveguide and cladding layers of the nRW-LD was well suppressed by the careful control of doping profile.
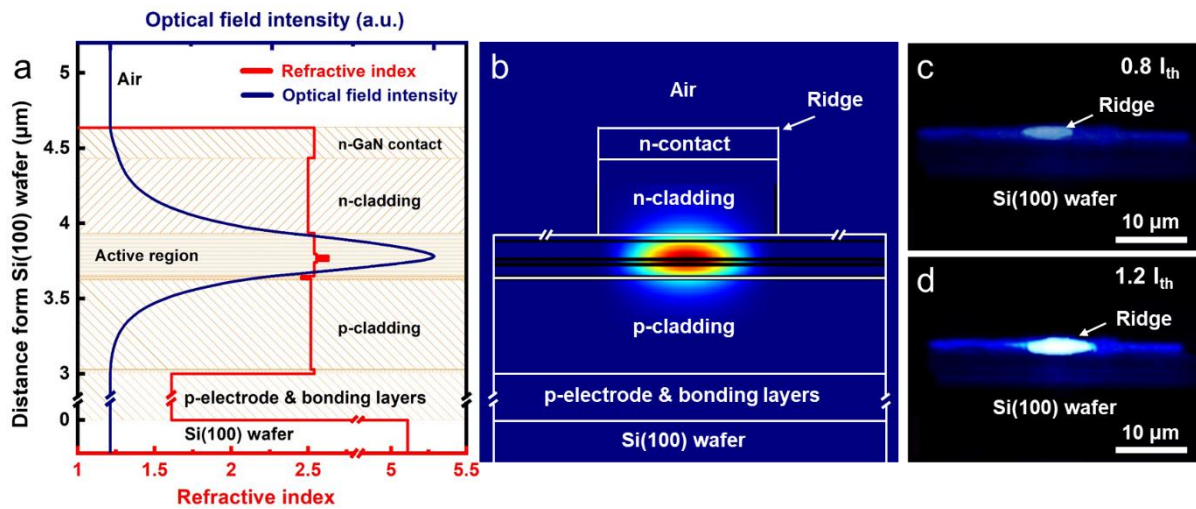

Figure S2: Simulated optical field distribution and observed NFPs of the as-fabricated InGaN-based nRW-LD. (a) Refractive index and optical field intensity profiles along the vertical direction as a function of distance from the Si(100) wafer.

The calculated optical field distribution (top axis) shows strong optical confinement around the active region. (b) Simulated optical field distribution. (c) and (d) Cross-sectional NFPs under an injection current of 0.8 I_{th} and 1.2 I_{th}, respectively.

Section 4: The detailed description for the measurement of junction temperature.

(1).The detailed description for the forward-voltage method :

For the measurement of the junction temperature of InGaN-based LDs, the forward-voltage method is based on the linear relationship between the inverse absolute temperature and natural logarithm of forward voltage subtracted by the turn-on voltage under current injection. The measured samples were put into an oven. When samples were operating under a pulsed injection current with 0.1% duty cycle (a pulse width of 0.1 μs and a repetition rate of 10 kHz), the self-heating effect due to the pulsed current was so small that it could be neglected, and the junction temperature was approximately equal to the ambient temperature. In this experiment, the pulsed injection current was set as the threshold current of 350 mA, and the corresponding forward voltage was recorded while the oven temperature was set at 22, 50, 60 and 70 °C, respectively. The turn-on voltage (V_0) was set as 3.0 V. And it is found that the dependence of In(V- V_0) on 1/T shows a good linearity. When the heat sink is kept at ambient temperature, the junction temperature under CW current injection can be calculated according to the recorded forward voltage based on the calibration curves.

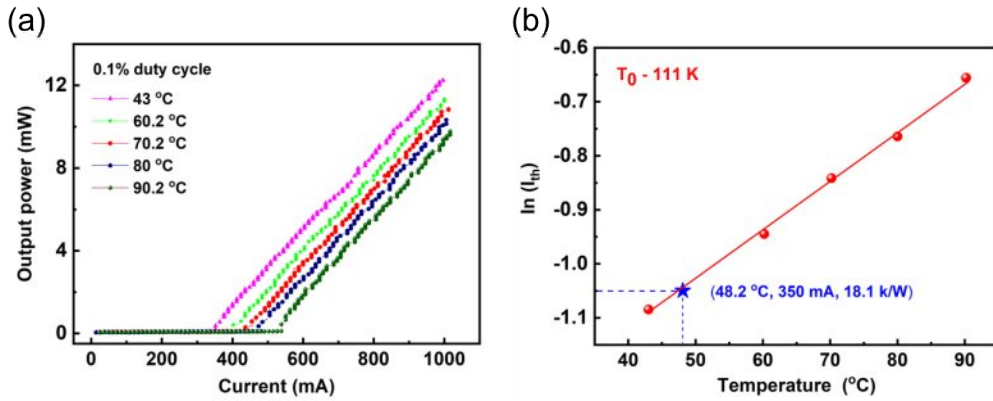(2).The detailed description for the threshold-current method :

Figure S3: The measurement of junction temperature for nRW-LD based on threshold-current method. (a) Light output power as a function of the pulsed injection current under various temperature. (b) The plot of $In(I_{th})$ as a function of temperature.

Figure S3 Shows the measurement of junction temperature for nRW-LD based on threshold-current method. The threshold current density J_{th} of LDs is dependent on temperature $J_{th} \propto e^{\frac{T}{T_0}}$. By using this relationship, the junction temperature can also be measured. Fig. S3a shows the P-I curves of the nRW-LD at various temperature. Combining the threshold current under various temperature, the calibration curve can be obtained as shown in Fig. S3b. Based on the linear relationship $In(I_{th}) \propto \frac{1}{T_0} \cdot T$, the characteristic temperature T_0 (~111 K) can be obtained. At the CW threshold current of 350 mA, the junction temperature of nRW-LD can be calculated to be 48.2 °C, which agrees well with the result obtained by the forward-voltage method (48.5 °C), implying a good validity and accuracy of the forward-voltage method.

Section 5: The statistic measurement results of the threshold currents of nRW-LDs.
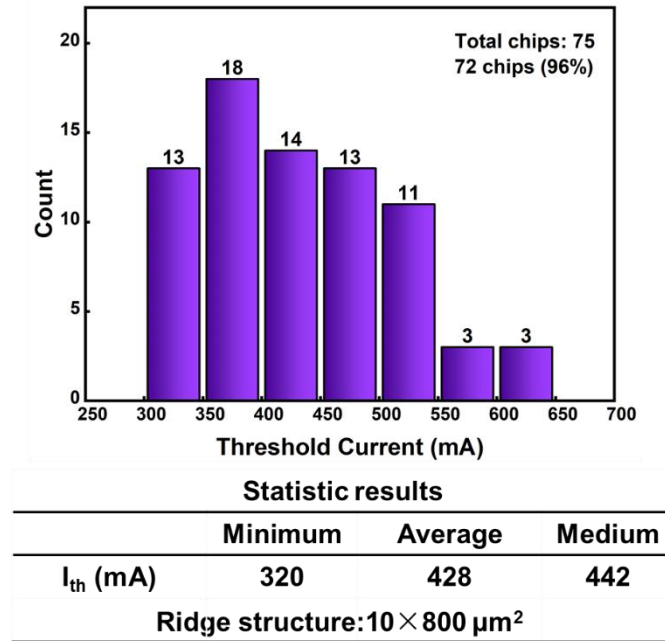

Figure S4: Statistic results of the threshold current for nRW-LDs.

In order to evaluate the yield and the reproducibility, we measured 75 as-fabricated nRW-LDs from the same epitaxial wafer. Figure S4 shows the statistic results for the threshold current of the nRW-LDs. The measurement was performed under pulsed current injection (pulse width of 400 ns and repetition rate of 10 kHz). 72 devices (96%) of the measured nRW-LDs can achieve lasing. The lowest, average and medium threshold currents were 320, 428 and 442 mA, respectively. These results exhibit a decent yield and reproducibility of the as-fabricated nRW-LDs.

Section 6: The detailed information of simulation study about thermal characteristics

Table S2: Detailed parameters for the thermal simulation of nRW-LD.

nRW-LD	Materials	Thickness (nm)	TC (W/mK)
Metal	Au	650	317
n-contact	GaN	200	130

n-cladding	n-$Al_{0.08}Ga_{0.92}$N/ u-$Al_{0.08}Ga_{0.92}$N	450/50	20
u-Waveguide	GaN	140	130
MQWs	$In_{0.12}Ga_{0.88}$N/ $In_{0.02}Ga_{0.98}$N	55.5	71
u-Waveguide	GaN	90	130
EBL	$Al_{0.18}G_{0.82}$N	20	14
p-cladding	$Al_{0.07}Ga_{0.93}$N	600	20
p-contact	GaN	30	130
Bonding metal	Ni-Sn solder	3000	55
Substrate	Si(100)	10^5	145
Heat sink	Cu	10^6	397

Table S3: Detailed parameters for the thermal simulation of pRW-LD.

pRW-LD	Materials	Thickness (nm)	TC (W/mK)
Metal	Au	650	317
p-contact	GaN	30	130
p-cladding	$Al_{0.07}Ga_{0.93}$N	600	20
EBL	$Al_{0.18}Ga_{0.82}$N	20	14
u-Waveguide	GaN	90	130
MQWs	$In_{0.12}Ga_{0.88}$N/ $In_{0.02}Ga_{0.98}$N	55.5	71
n-Waveguide	GaN	100	130
n-cladding	$Al_{0.08}Ga_{0.92}$N	1200	20
n-contact	GaN	1300	130
Buffer layer	$Al_{0.17}Ga_{0.83}$N/ $Al_{0.35}Ga_{0.65}$N/ AlN	400/300/300	14/10/170
Substrate	Si(111)	10^5	145
Heat sink	Cu	10^6	397

Simulation study based finite element method was adopted to compare the junction temperature and thermal resistance of the InGaN-based nRW-LD and pRW-LD after simple package. The detailed information of thickness and thermal conductivity for each layer is shown in Tables S2 and S3. For the pRW-LD, the operating voltage and

current were 5.56 V and 350 mA, respectively. For the nRW-LD, the operating voltage

and current were 4.15 V and 350 mA, respectively. The light output power was in the

milliwatt range. And the ambient temperature was set at 22 $^{\circ}$C in the simulation,

assuming that the heat distributed uniformly in the p-type layers and the active region.

Simulation results show that the junction temperature rise of the pRW-LD was 52.1 $^{\circ}$C,

and the thermal resistance was calculated to be 26.8 K/W. The junction temperature

rise of nRW-LD was 26.7 $^{\circ}$C, and the thermal resistance was 18.4 K/W. By replacing

the Ni-Sn bonding material for nRW-LD with copper, the junction temperature rise of

pRW-LD would be only 19.2 $^{\circ}$C and the thermal resistance 13.2 K/W. The simulation

results confirmed InGaN-based nRW-LDs have a huge prospect in thermal

characteristics, which would boost the device performance.